CrossMark

New Observational $H(z)$ Data from Full-spectrum Fitting of Cosmic Chronometers in the LEGA-C Survey

Kang Jiao[1,2,3] ⓘ, Nicola Borghi[3,4] ⓘ, Michele Moresco[3,4] ⓘ, and Tong-Jie Zhang[1,2,5] ⓘ

[1] Institute for Frontiers in Astronomy and Astrophysics, Beijing Normal University, Beijing 102206, People's Republic of China; tjzhang@bnu.edu.cn
[2] Department of Astronomy, Beijing Normal University, Beijing 100875, People's Republic of China
[3] Dipartimento di Fisica e Astronomia "Augusto Righi", Alma Mater Studiorum Università di Bologna, via Piero Gobetti 93/2, I-40129 Bologna, Italy
michele.moresco@unibo.it
[4] INAF—Osservatorio di Astrofisica e Scienza dello Spazio di Bologna, via Piero Gobetti 93/3, I-40129 Bologna, Italy
[5] Institute for Astronomical Science, Dezhou University, Dezhou 253023, People's Republic of China

Abstract

In this work, we perform a full-spectrum fitting of 350 massive and passive galaxies selected as cosmic chronometers from the LEGA-C ESO public survey to derive their stellar ages, metallicities, and star formation histories. We extensively test our results by assessing their dependence on the possible contribution of dust, calibration of noise and signal, and use of photometric data in addition to spectral information; we also identify indicators of the correct convergence of the results, including the shape of the posterior distributions, the analysis of specific spectral features, and the correct reproduction of the observed spectrum. We derive a clear age–redshift trend compatible with the aging in a standard cosmological model showing a clear downsizing pattern, with more massive galaxies being formed at higher redshift ($z_f \sim 2.5$) with respect to less massive ones ($z_f \sim 2$). From these data, we measure the differential aging of this population of cosmic chronometers to derive a new measurement of the Hubble parameter, obtaining $H(z = 0.8) = 113.1 \pm 15.1(\text{stat.})^{+29.1}_{-11.3}(\text{syst.})$. This analysis allows us to compare for the first time the differential ages of cosmic chronometers measured on the same sample with two completely different methods, the full-spectrum fit (this work) and the analysis of Lick indices, known to correlate with the age and metallicity of the stellar populations. Albeit an understood offset in the absolute ages, the differential ages have proven to be extremely compatible between the two methods, despite the very different data, assumptions, and models considered, demonstrating the robustness of the method.

Unified Astronomy Thesaurus concepts: Cosmological evolution (336); Observational cosmology (1146); Galaxy ages (576)

1. Introduction

Since the discovery of the accelerating expansion of the universe (Riess et al. 1998; Perlmutter et al. 1999), the cosmological community has been working to understand the mechanism of this expansion. Modern cosmology postulates that dark energy, an unknown form of energy with negative pressure, is driving the accelerated expansion of the late universe and that the gravitational effect of cold dark matter (CDM) shapes the large-scale structure of the universe, a model dubbed ΛCDM. Numerous cosmological probes and observations, including the cosmic microwave background (CMB; e.g., Smoot et al. 1992; Bennett et al. 2003; Carlstrom et al. 2011; Swetz et al. 2011; Planck Collaboration et al. 2014, 2020), baryon acoustic oscillations (BAOs; e.g., Percival et al. 2001; Cole et al. 2005; Eisenstein et al. 2005), Type Ia supernovae (SNe; e.g., Sullivan et al. 2011; Suzuki et al. 2012; Betoule et al. 2014; Scolnic et al. 2018), weak gravitational lensing (Bartelmann & Schneider 2001), and cluster counts (Allen et al. 2011), have been proposed and extensively studied to determine the universe's large-scale structure and evolution. After more than 20 yr of unremitting efforts, we are now in the golden age of precision cosmology, with measurements and constraints on cosmological parameters reaching the percent level.

The Hubble constant H_0 has long been a critical observable of observational cosmology (Freedman & Madore 2010), and its value is directly related to our current estimate of the universe's age. However, the two probes that represent the most precise level of measurement today, SNe and the CMB, produce significant discrepancies beyond the order of 4σ (for an extensive review, see Di Valentino et al. 2021). The increase of observational evidence supporting this discrepancy between observations of the early and late universe has undoubtedly kicked off a crisis in modern cosmology (Davis 2019; Verde et al. 2019; Riess 2020; Abdalla et al. 2022). At the moment, there are suggested theories to try to explain it, even if they are not definitive (Di Valentino et al. 2021). Alternative cosmological probes (Moresco et al. 2022) can play an important role in obtaining additional independent, high-precision measurements to assess the current Hubble tension's reliability. It also becomes evident that a single probe is not adequate to constrain the properties and evolution of the universe accurately and completely. The Hubble parameter $H(z)$ is the physical quantity that most directly describes the history of the universe's expansion, and its measurement has advanced significantly over the last decade or so. We can not only reconstruct these $H(z)$ measurements to extrapolate H_0 at zero redshift, shedding light on a different path to explore the crisis, but also enhance our ability to understand the nature of dark energy, which dominates the late universe just covered by the observable range of $H(z)$.

Existing observational $H(z)$ data (referred to as OHD; see, e.g., Zhang et al. 2010; Ma & Zhang 2011) are mainly based on two probes: the differential age method and the radial BAO size method (Benitez et al. 2009). The first method can be obtained with cosmic chronometers (CCs; Jimenez & Loeb 2002; Moresco et al. 2018, 2020) by measuring the differential age–redshift relation of massive and passive galaxies throughout the universe. Any systematic offset introduced by the galaxy age measurement method will be canceled out when deriving the differential age. A total of 32 $H(z)$ measurements have been obtained (Jimenez et al. 2003; Simon et al. 2005; Stern et al. 2010; Moresco et al. 2012; Zhang et al. 2014; Moresco 2015; Moresco et al. 2016; Ratsimbazafy et al. 2017; Borghi et al. 2022b) and are currently widely used to test cosmological models. These measurements are regarded as cosmological model–independent, since the principle is not dependent on the choice of cosmological models. The second method is based on the inverse proportionality between $H(z)$ and the differential radial (comoving) distance, which can be traced by measuring the radial size of BAO features at different redshifts. This method, however, requires knowledge of the comoving BAO scale (r_{BAO}), which is derived from the CMB measurements. This fact makes this probe not fully cosmology-independent, since typically in the derivation of the sound horizon scale from CMB, a cosmology model is assumed. Additionally, gravitational waves can be used as standard sirens (Schutz 1986; Holz & Hughes 2005; Abbott et al. 2017) to study $H(z)$, with promising perspectives for the next decade (Farr et al. 2019). Finally, the phenomenal growth of fast radio burst observations also expands the $H(z)$ measurement possibilities (Wu et al. 2020).

Selecting a pure passive sample and measuring the age difference between galaxies are the two bases of the CC method. Various strategies have been proposed to distinguish "passive" from "star-forming" galaxies, including morphological selections of spheroidal systems (following Hubble 1936), cuts on color–color diagrams (e.g., UVJ, Williams et al. 2009; $NUVrJ$, Ilbert et al. 2013) or a color–mass diagram (e.g., Peng et al. 2010), and spectral energy distribution (SED) fitting (e.g., Pozzetti et al. 2010). Combining multiple criteria and maximizing the overlap of complementary information (photometric and spectroscopic) result in a significantly more effective method of selecting a pure sample (Moresco et al. 2013, 2018; Borghi et al. 2022a). While spectral line analysis enables us to obtain extremely precise redshift values, the situation is much more complicated in determining the age, which cannot be directly observed but can be estimated using photometry (SED), single spectral regions (e.g., D4000, Lick indices), or the entire spectrum's features (full spectral fitting). However, each of these methods may suffer various systematics caused by parameter degeneracies. Moresco (2011) explained that SED fitting, which is commonly used to derive galaxies' ages, is incapable of fully breaking the age–metallicity degeneracy; also, the age degenerates to τ in the delayed exponential star formation history (SFH). Moresco et al. (2011) proposed an innovative method that consists of using not the age but rather a direct spectroscopic observable (the 4000 Å break) to measure $H(z)$, making the decoupling of systematic and statistical errors easier. Most recently, Borghi et al. (2022b) obtained for the first time a new $H(z)$ measurement using the Lick index method. Their analysis takes advantage of the high signal-to-noise ratio (S/N)

spectroscopic data of the Large Early Galaxy Astrophysics Census (LEGA-C) DR2 survey (Straatman et al. 2018) of galaxies at $z \sim 0.7$. However, the Lick index method does not allow one to flexibly study the galaxies' SFHs, which are useful to better exclude possible biases in the derived age–redshift relation and, therefore, on $H(z)$. For the purpose of optimizing the set of spectral absorption features for Lick index fitting, Borghi et al. (2022b) only made use of a subsample (140 galaxies) of the selected passive sample, while the full-spectrum fitting is not subject to this issue.

In this paper, we perform full-spectrum fitting to derive the ages and SFHs of passive galaxies in LEGA-C DR2, then use them as CCs to obtain a new $H(z)$ measurement. The data set is introduced in Section 2, and the fundamental principles and details of the full-spectrum fitting are in Section 3. In Section 4, we present the results on physical parameters and strategies to improve the performance of their estimation. In Section 5, we detail the procedure for applying the CC method and presenting and discussing the final $H(z)$ measurement results. The conclusions are presented in Section 6.

2. Data

In this section, we describe the spectroscopic and photometric data used in this analysis and the selection criteria adopted to select the sample of CCs.

Spectroscopic data. The spectroscopic data are taken from LEGA-C, an ESO 130-night public survey of $\sim$3200 K_s-band selected galaxies conducted with VIMOS (Le Fèvre et al. 2003) on the Very Large Telescope. The 20 hr long integrations produce continuum spectra with an average S/N ~ 21.8 pixel^{-1} (0.6 Å) for massive galaxies ($M \gtrsim 10^{11}\ M_\odot$). The second data release (LEGA-C DR2; Straatman et al. 2018) includes 1988 spectra in the redshift range $0.6 \lesssim z \lesssim 1.0$ covering the observed wavelength range of $\sim$6300–8800 Å with an effective spectral resolution of $R \sim 3500$. We add the spectral index measurements from Borghi et al. (2022a) to the LEGA-C data set, providing a catalog of Lick index measurements including the recent Ca II H/K diagnostic (a useful tracer of recent episodes of star formation; Moresco et al. 2018).

Photometric data. One of the advantages of the LEGA-C sources is that, being observed in the COSMOS field, a wealth of multiwavelength photometric observations are available (e.g., Muzzin et al. 2013; Laigle et al. 2016; Weaver et al. 2022). In this work, following Straatman et al. (2018), we adopt the Ultra Deep Survey with the VISTA telescope (UltraVISTA) photometric catalog from Muzzin et al. (2013). We use a total of 21 photometric bands, namely, IB427, IB464, IA484, IB505, IA527, IB574, IA624, IA679, IB709, IA738, IA767, IB827, *u*, *V*, *zp*, *Y*, *J*, *H*, *Ks*, *ch1*, and *ch2*. For a given filter *x*, we compute the total flux $f_{x,\mathrm{tot}}$ by applying the equation

$$f_{x,\mathrm{tot}} = f_x \times \frac{f_{K_s,\mathrm{tot}}}{f_{K_s}}, \qquad (1)$$

where $f_{K_s,\mathrm{tot}}$ is the total K_s-band flux from SExtractor's *flux_auto* that has been corrected using the growth curve of the point-spread function stars, and f_{K_s} is the specific K_s-band flux (see Muzzin et al. 2013). The SEDs of the catalogs are in good agreement, but differences in calibration and measurement precision may affect the age–*z* relation. We will further explore
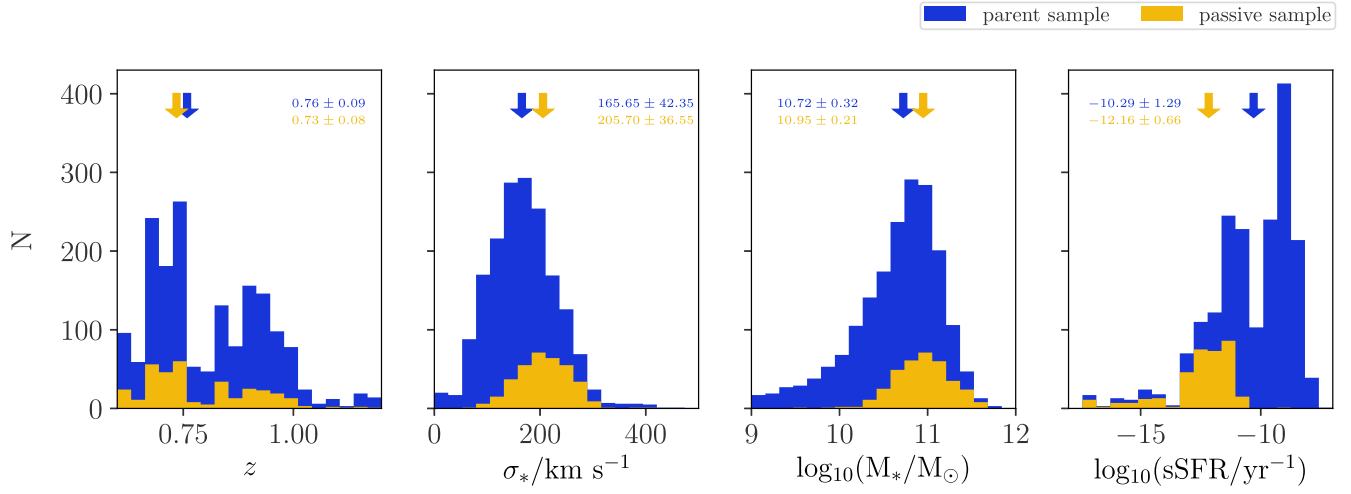
Figure 1. Distributions of four key parameters for the LEGA-C DR2 parent sample (blue) and the 350 passive galaxies analyzed in this work (yellow). The redshift (z), stellar velocity dispersion ($\sigma_\star$), and stellar mass ($M_\star$) are taken from LEGA-C DR2, while the sSFRs are from COSMOS2015. The arrows mark out the median values.

the use of different photometric catalogs in a follow-up analysis.

The sample. By combining *NUVrJ* selection, a cut based on the equivalent width of the [O II] $\lambda3727$ line of <5 Å, and a visual inspection to further remove galaxies with strong [O II] $\lambda3727$ and/or [O III] $\lambda5007$ emission lines, Borghi et al. (2022a) selected a pure sample of 350 passive galaxies in LEGA-C DR2, minimizing any residual contamination from star-forming outliers. The distribution of some key parameters describing this population is shown in Figure 1. This passive sample has a median redshift of $\langle z \rangle = 0.735$ with two peaks around $z \sim 0.745$ and 0.839. The median values of the $\sigma_\star$ and $\log_{10}(M_\star/M_\odot)$ distributions increase from 165.7 (10.72) to 205.7 (10.95) km s^{-1}, respectively. The specific star formation rate (sSFR) distribution has a median logarithmic value of $\langle \log_{10}(\mathrm{sSFR}) \rangle = -12.2$ yr^{-1}, which is ~1 dex lower than what is typically used to define a galaxy as "passive" (e.g., Pozzetti et al. 2010).

3. Method

Full-spectrum fitting. To perform the full-spectrum fitting, we use the BAGPIPES code developed by Carnall et al. (2018). BAGPIPES models the observed spectrum of a galaxy f_{obs} into $f^{\mathcal{H}}(\Theta)$ based on a hypothesis $\mathcal{H}$ of the physics involved described by parameters Θ. The posterior distribution $P(\Theta|f_\lambda, \mathcal{H})$ obtained from the Bayes theorem,

$$P(\Theta|f_\lambda, \mathcal{H}) = \frac{\mathcal{L}(f_\lambda|\Theta, \mathcal{H})P(\Theta|\mathcal{H})}{P(f_\lambda|\mathcal{H})}, \quad (2)$$

is sampled with the nested sampling algorithm MULTINEST (Buchner et al. 2014). Here $\mathcal{H}$ includes the modeling of the star formation rate (SFR; $t_{\mathrm{U}i}$), the simple stellar population (SSP; t_i, λ, Z_j), and the neutral and ionized interstellar medium radiative transmission functions $T^0(t_i, \lambda)$ and $T^+(t_i, \lambda)$, which

are used to simulate the luminosity function of a galaxy,

$$L_\lambda = \sum_{j=1}^{N_c}\sum_{i=1}^{N_a} \mathrm{SFR}_j(t_{\mathrm{U}i})\, \mathrm{SSP}(t_{\mathrm{U}i}, \lambda, Z_j)$$
$$\times\, T^+(t_i, \lambda)\, T^0(t_i, \lambda)\, \Delta t_i, \quad (3)$$

where t_{U}, t, λ, and Z are the cosmic time, the age of the stellar population, the wavelength of the spectral line, and the stellar metallicity, respectively, and the subscripts i and j denote summations for all of the age bins and SFH components, respectively. Here $\mathcal{H}$ also includes the modeling of the intergalactic medium (IGM) radiative transfer to finally simulate the observed flux,

$$f_{\lambda_{\mathrm{obs}}} = \frac{L_\lambda}{4\pi D_L(z_{\mathrm{obs}})^2(1 + z_{\mathrm{obs}})}T_{\mathrm{IGM}}(\lambda, z_{\mathrm{obs}}), \quad (4)$$

where $\lambda_{\mathrm{obs}} = (1 + z_{\mathrm{obs}})\lambda$, $D_L(z_{\mathrm{obs}})$ is the luminosity distance, and T_{IGM} is the transmission function of the IGM. The nebular emission lines and continuum come from precomputed CLOUDY (Ferland et al. 2017) grids with only one free parameter, the logarithmic ionization parameter ($\log_{10}(U)$). We apply the Charlot & Fall (2000) model out of the four choices of dust attenuation models (see detailed descriptions in Carnall et al. 2018) that BAGPIPES provides. The likelihood function can be written in a logarithmic form as

$$\ln(\mathcal{L}) = -0.5\sum_i \ln(2\pi\sigma_i^2) - 0.5\sum_i \frac{(f_i - f_i^{\mathcal{H}}(\Theta))^2}{\sigma_i^2}, \quad (5)$$

where σ is the observation error of the fluxes and sums over all ith wavelength pixels.

In addition to the spectrum, BAGPIPES allows the inclusion of photometric data points in the fit, thus enabling modeling of a galaxy SED on a wide wavelength range from far-ultraviolet to microwave regimes. Another significant advantage is that it

is possible to adaptively test different SFH choices (e.g., single burst, constant, and exponentially declining, as well as a combination of them). Models within the BAGPIPES code are resampled in an age grid Δt_i based on the SSP model generated using the 2016 version of the Bruzual & Charlot (2003) models. BAGPIPES is structured around three core classes, which are `galaxy` for loading observational data, `model_galaxy` for generating model galaxy spectra, and `fit` for fitting models to observational data. The code is open source and publicly available.[6] To extract parameter values and associated uncertainties from the posterior distributions, we adopt the median and 16th–84th percentiles, respectively.

SFH choice. Most of the CC analyses, including Borghi et al. (2022b), assume single-burst SFHs as an ideal simplification of the real SFH. This model assumes that the total mass of a galaxy suddenly formed at a specific cosmic time, which is characterized by a delta function $SFR(t_U) \propto \delta(t_U)$. A more realistic SFH model is necessary to test the robustness of the age–z relations and the $H(z)$ obtained. In this work, we extend this analysis by testing two other well-established SFH models, namely, the double power-law (DPL) and delayed exponentially declining (DED) models, based on the CC sample that Borghi et al. (2022a) compiled. The DPL model separates the rising and declining phases of the SFH using two separate power-law slopes, $SFR(t_U) \propto [(t_U/\tau)^{\alpha} + (t_U/\tau)^{-\beta}]^{-1}$, where α is the falling slope, β is the rising slope, and τ is related to (but not the same as) the peak time. The DED model assumes that the star formation starts at some time T_0 and increases gradually to its peak, after which it declines exponentially with some timescale τ,

$$
SFR(t_U) \propto
\begin{cases}
(t_U - T_0)\exp\left(-\dfrac{t_U - T_0}{\tau}\right) & t_U > T_0 \\
0 & t_U < T_0
\end{cases}.
\tag{6}
$$

As detailed in this section, we fit the selected sample separately using the DPL and DED models and get compatible median reduced χ^2 values for the spectrum of $\chi_\nu^2 = 1.96$ and 1.92. According to the principle of Occam's razor, we choose the one fewer free parameter model—DED (Equation (6)) for the following analysis.

Removing the cosmological prior. The age of a stellar population, t, is defined as the lookback time between its observed redshift and the beginning of its star formation,

$$
t \equiv t_U(z_{obs}) - t_{U,start}.
\tag{7}
$$

In fact, the cosmic time (t_U) at a given redshift is not a direct observable; we can only calculate its value based on a cosmological model. BAGPIPES use ΛCDM as its default cosmological model with the default parameters $\Omega_M = 0.3$, $\Omega_\Lambda = 0.7$, and $H_0 = 70$ km s^{-1} Mpc^{-1}. In principle, when the age of a galaxy exceeds the age of the universe, it is reasonable to consider it nonphysical. To address this issue, BAGPIPES assumes that the $SFR(t_{Ui}) = 0$ when the retrieved age is larger than the estimated age of the universe at the given redshift. While this assumption is typically neglected in galaxy evolution studies, being of relative interest for the results,

---

[6] https://github.com/ACCarnall/bagpipes

imposing an upper limit on the retrieved age based on a cosmological model is to be strictly avoided in our analysis. In particular, such a prior could induce cosmological biases in the age estimates and circular arguments in the derivation of the Hubble parameter, since if the ages of the oldest objects are set to the age of the universe of the reference cosmological model, the method would artificially provide, by definition, the reference cosmology.

Fortunately, we can avoid the above situation by releasing the upper limit for t_U in BAGPIPES to a value that our sample galaxies cannot exceed, such as 20 Gyr at all redshifts. This modification changes the upper boundary of the age sampling without affecting the sampling grid. Galaxies' ages can be easily retrieved by subtracting the formation time from the new upper limit we set, and the age–z slope will not be affected by the cosmological assumptions. Besides, we notice that the cosmological model is also used when calculating the D_L in Equation (4). The D_L does not interact with t_U in the rest of the code, and because of the negligible dependence of $dH(z) \sim \mathcal{O}^2(dD_L)$, it is acceptable to ignore the issue of D_L affected by the choice of cosmological model (see Figure 1 in Jimenez & Loeb 2002). In conclusion, with these modifications, we "erase" the effect of the cosmological prior on the galaxy age estimation in the original BAGPIPES code.
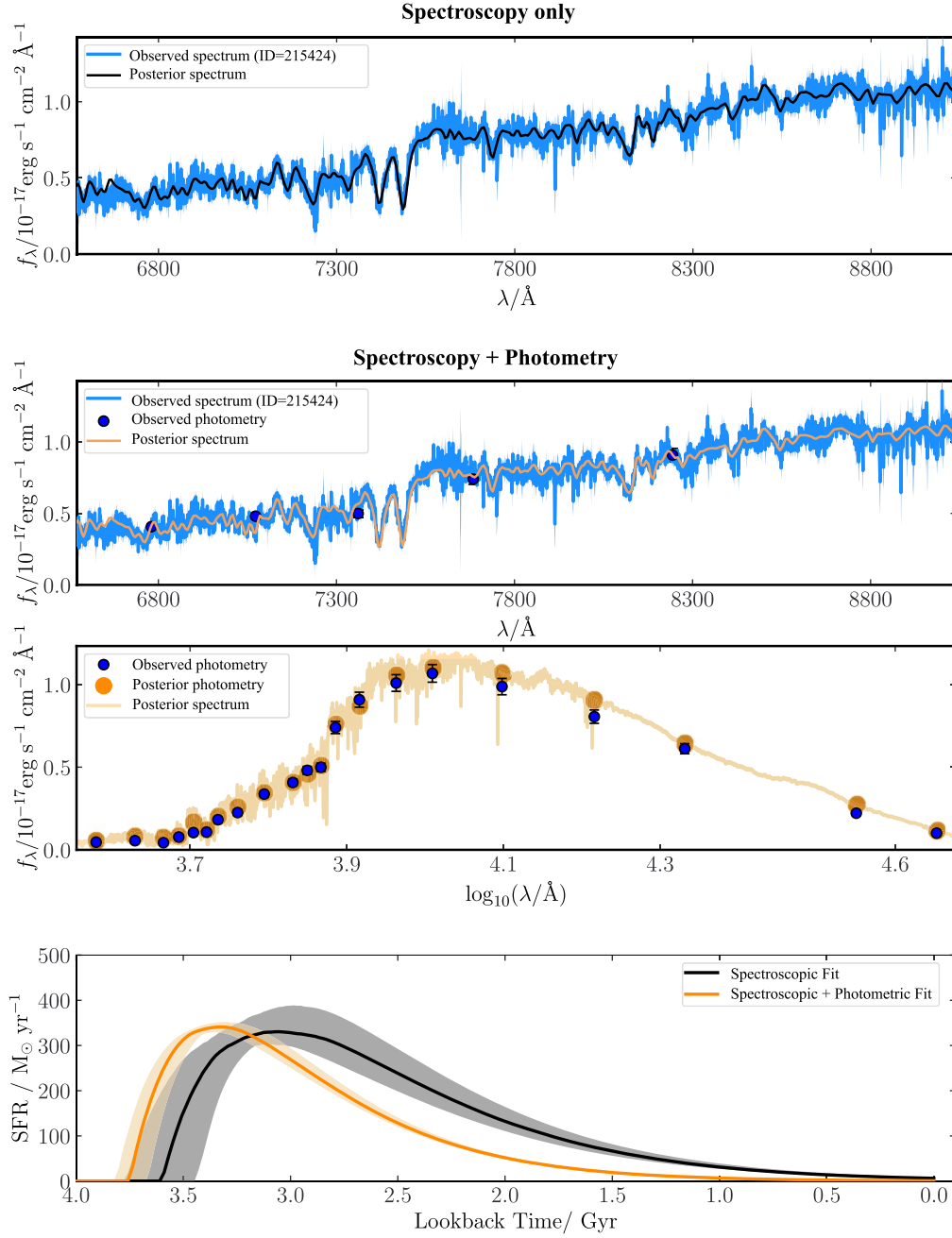
Adding photometric data. The spectroscopy covers a relatively narrow wavelength range of the galaxies' entire spectrum compared with the photometry. Fitting spectroscopic data alone, due to the lack of enough information, is incapable of fully modeling the line features and breaking the degeneracy between parameters, especially the age–τ degeneracy in our analysis, as well as the Ca II H and K lines that are essential for diagnostic of passive galaxies. Adding photometric data will improve the performance of fitting by providing additional information. We employ the K_s-selected UltraVISTA photometries in our analysis as detailed in Section 2.

In Figure 2, we show the full-spectrum fitting results from an example galaxy (ID 215424) obtained with spectroscopic data alone and adding photometry. We observe that in the posterior, the Ca II K line is less deep than the H line for the spectroscopic (only) fitting, contradicting the observational data. On the contrary, this feature is well reproduced after including the photometric data in the fit. This same behavior is observed, in general, for the entire sample. In particular, the median percentage difference between the observed and reconstructed H/K (see also Table 1 and Section 4.1 for a more extended discussion) is significantly reduced from the value of $11.93\% \pm 6.76\%$–$6.46\% \pm 4.34\%$. From the histograms in Figure 3, we observe both long tails of derived ages and τ distributions for the spectroscopic (only) fitting, indicating the existence of the age–τ degeneracy, while the tails are significantly suppressed after adding the photometric fitting.

Exploring parameter space. In our analysis, we fully explore all of the possible parameter space consisting of the physical properties of the galaxy, the parameters of modeling the noise, and the dust attenuation, together with the calibration of the fluxes. We consider two diagnostics, the reduced χ^2 (χ_ν^2) and the percentage difference of H/K (see topical description in Section 4.1), to quantify the agreement between the posterior and observed spectrum and verify the improvement of the fit when adding more information on the parameters.

Fitting redshift is not necessary; for each galaxy, we set its z to the value of the high-precision spectroscopic redshift derived

Figure 2. Full-spectrum fitting results for an example galaxy (ID = 215424) obtained with spectroscopic data alone (first panel) and adding photometry (second and third panels). The observational spectra from LEGA-C DR2 (Straatman et al. 2018) and photometric data points from the UltraVISTA catalog of Muzzin et al. (2013) are shown in light and dark blue, respectively. The best-fit BAGPIPES spectra and photometric points from fitting spectroscopy and spectroscopy+photometry are shown in black and orange, respectively. The fourth panel shows the best-fit BAGPIPES SFR (as a function of lookback time); the solid curves are the median posteriors, the shaded regions are the 1σ confidence regions, and the horizontal axis is the lookback time since $t(z_{\rm obs})$.

from numerous high-S/N absorption features observed in the LEGA-C DR2 spectra. We take uniform priors in reasonably wide parameter spaces for the age (t), star formation timescale (τ), stellar metallicity (Z), and log of the mass formed $\log_{10}(M_{\rm form})$ as described in Table 1. The stellar velocity dispersion $\sigma_\star$ is a direct observable derived from the line broadening of the spectrum; we test the effect of using a wide uninformative prior $\sigma_\star \sim \mathcal{U}[0, 400]$ and narrower Gaussian prior of $\sigma_\star \sim \mathcal{G}[\sigma_\star; err_{\sigma_\star}]$, set by the measurements provided in the LEGA-C DR2 catalog. We also test the impact of varying the observed flux calibration according to a second-order Chebyshev polynomial with the coefficients' prior set to

$P_0 \sim \mathcal{G}[1, 0.25]$, $P_1 \sim \mathcal{G}[0, 0.25]$, and $P_2 \sim \mathcal{G}[0, 0.25]$ for each of the orders, respectively. We also test the white-noise model as an additional component by adopting a uniform prior for the logarithmic white-noise scaling parameter $\log_{10}(S_{\rm noise}) \sim \mathcal{U}[0, 10]$. Finally, even if we expect it to be negligible for this sample, we additionally model the dust effect by assuming the Calzetti et al. (2000) attenuation curve and a Gaussian prior on the absolute attenuation at 5500 Å, $A_V \sim \mathcal{G}[1, 0.25]$, a multiplicative factor of $\eta = 2$ for stars in birth clouds, and an attenuation power-law slope of $n \sim \mathcal{G}[0.7, 0.3]$ in the range $n \in [0.3, 2.5]$. For further details on each model component, see Carnall et al. (2018). When

Table 1
Model Ingredients for the Various Analyses Performed

z	t/Gyr	τ/Gyr	Z/Z☉	log($M_{form}/M_\odot$)	$\sigma_\star$/km s⁻¹	Calib.	Noise	Dust	Photo. 21 Bands	$\langle \chi_\nu^2 \rangle$	$\langle \Delta \, H/K \rangle$ (%)
Fixed	$\mathcal{U}[0, 20]$	$\mathcal{U}[0, 2]$	$\mathcal{U}[0.001, 3]$	$\mathcal{U}[0, 18]$	$\mathcal{G}[\sigma_\star; \mathrm{err}_{\sigma_\star}]$						
(1)	(2)	(3)	(4)	(5)	(6)	(7)	(8)	(9)	(10)	(11)	(12)
·	·	·	·	·	·	×	·	·	×	1.95 ± 0.44	11.93 ± 6.76
·	·	·	·	·	·	·	·	×	·	1.96 ± 0.45	9.66 ± 5.94
·	·	·	·	·	·	·	·	·	·	1.93 ± 0.43	7.99 ± 5.34
·	·	·	·	·	×	·	·	·	·	1.93 ± 0.43	7.83 ± 5.17
·	·	·	·	·	·	·	×	·	·	1.93 ± 0.43	6.58 ± 4.08
·	·	·	·	·	·	×	·	·	·	1.97 ± 0.45	6.46 ± 4.34

Note. The · and × mark the use or not of the corresponding prior (columns (1)–(6); see Section 3), the model components (columns (7)–(9); three-order polynomial calibration, white noise, and the Calzetti et al. 2000 dust attenuation model), and the photometric data (column 10; see Section 2). The $\langle \chi_\nu^2 \rangle$ and $\langle \Delta \, H/K \rangle$ are the median ± median absolute deviation of the distributions taking account of the 350 fitting results.

doing the analyses, we do not expect the nebular and dust emission modelings to have significant impacts on our results, since our galaxies were selected to have negligible or no emission line contribution (Borghi et al. 2022b).

We compare the results obtained from using or not using the aforementioned components and find that all of the $\langle \chi_\nu^2 \rangle$ are compatible (on the second digits). The modeling of H/K (see topical description in Section 4.1) is significantly improved (on the first digits of $\langle \Delta \, H/K \rangle$) when not using the calibration or modeling the noise. Since the LEGA-C DR2 spectra are flux calibrated using UltraVISTA's photometric SEDs, we prefer not to impact on the data with an additional calibration. But the other option is also acceptable, and we get compatible $H(z)$ measurements for them during the following step analyses. We decide to use as a baseline the set of parameters that better reproduces the Ca II H/K feature (the last row of Table 1, since it has been proven to be a very powerful and important diagnostic to trace the purity of CC samples; see Moresco et al. 2018; Borghi et al. 2022a; Moresco et al. 2022), and having a significantly different H/K in the reconstructed spectrum would mean not correctly reproducing the behavior of our data, possibly resulting in biases in the results. Moreover, we notice that all of the models present a compatible χ_ν^2, but this model also has the advantage of avoiding additional calibration, since the LEGA-C DR2 spectra are flux calibrated using UltraVISTA's photometric data.

4. Analysis

In this section, we present our analysis of the physical parameters derived. We start by defining three diagnostic criteria to assess the reliability of our results and flag the constraints not properly converged. We will explore their use to improve the robustness of the derived parameter, if needed, concluding by presenting the baseline results on which the cosmological analysis will be based.

4.1. Breaking the Degeneracies

In Figure 3, we present the distributions of the derived parameters (z, $\sigma_\star$, stellar age, and τ) obtained from our analysis of both the spectroscopic data alone and the fit of the spectroscopic and photometric data combined. We start by observing that the pure spectroscopic case presents significant tails in the age and τ distributions, with ages larger than the age of the universe and τ up to the maximum value allowed by the prior. We will therefore define a set of diagnostic criteria to

check the accuracy of our results, apply them to our constraints, and verify if and how they can impact the nonphysical large values just discussed.

Improperly converged constraints. The values estimated from the posterior distributions obtained from BAGPIPES may not be fully reliable, depending on several issues. As an example, this is the case when the posterior distribution exhibits multimodal peaks, or is very skewed toward the edge of the domain allowed by the priors. Considering the large number of galaxies and combinations of parameters explored, we develop two efficient automatic algorithms to assist us in recognizing these issues and subsequently flagging the corresponding galaxies.

We identify the multimodality by counting the convex inflection points of the one-dimensional posterior distribution functions (PDFs) after applying a Gaussian kernel smoothing function with a bandwidth with size 12% of the full posterior range. This technique is robust against spurious detection of close-by peaks in distributions that are not significantly multimodal. We validate this method through visual inspection, verifying that PDFs with zero inflection points are actually very flat and uninformative, and those with more than one are significantly multimodal. Therefore, we keep those PDFs with only one convex inflection point. Throughout the paper, we refer to this specific flag as `unimodal`.

To determine whether a posterior is very skewed toward the parameter space boundary, the most intuitive method is to examine whether the estimated upper and lower bounds exceed the parameter space. Here we adopt a more flexible approach based on the skewness computed as the adjusted Fisher–Pearson standardized moment coefficient of the PDF; if the absolute value of the skewness is >1, the chain is considered highly skewed or asymmetric, indicating that it is converging toward the edge of the parameter space. We validate this algorithm by visually inspecting the one-dimensional posterior PDFs of a fully fitted catalog. Throughout the paper, we refer to this specific flag as `not truncated`.

In our Bayesian analysis, there are numerous free parameters involved, including the model components of noise and dust as discussed in Section 3, for which, in principle, one may apply these automatic inspection techniques. In this work, we consider only four key parameters associated with the galaxies' physical properties, namely, age, τ, Z, and $M_\star$. The final `unimodal` (or `not truncated`) flag is then taken from the intersection (AND logic) of the individual flags obtained from all four parameters.

## Spectroscopic (only) Fit
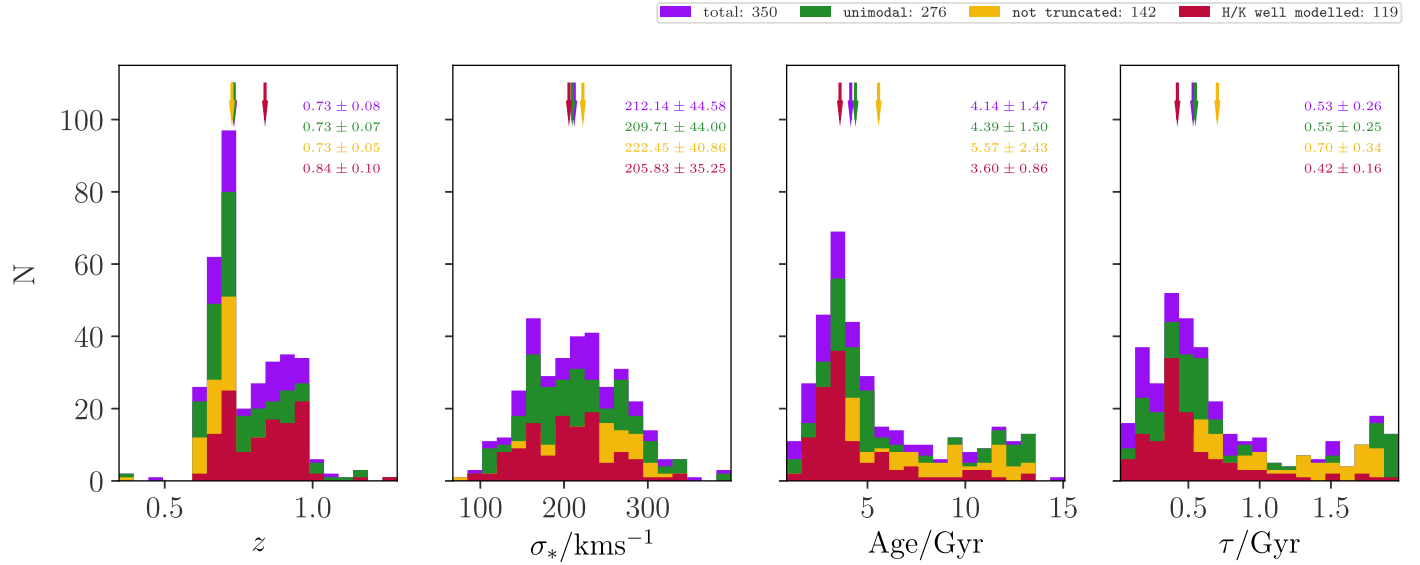
Spectroscopic + Photometric Fit
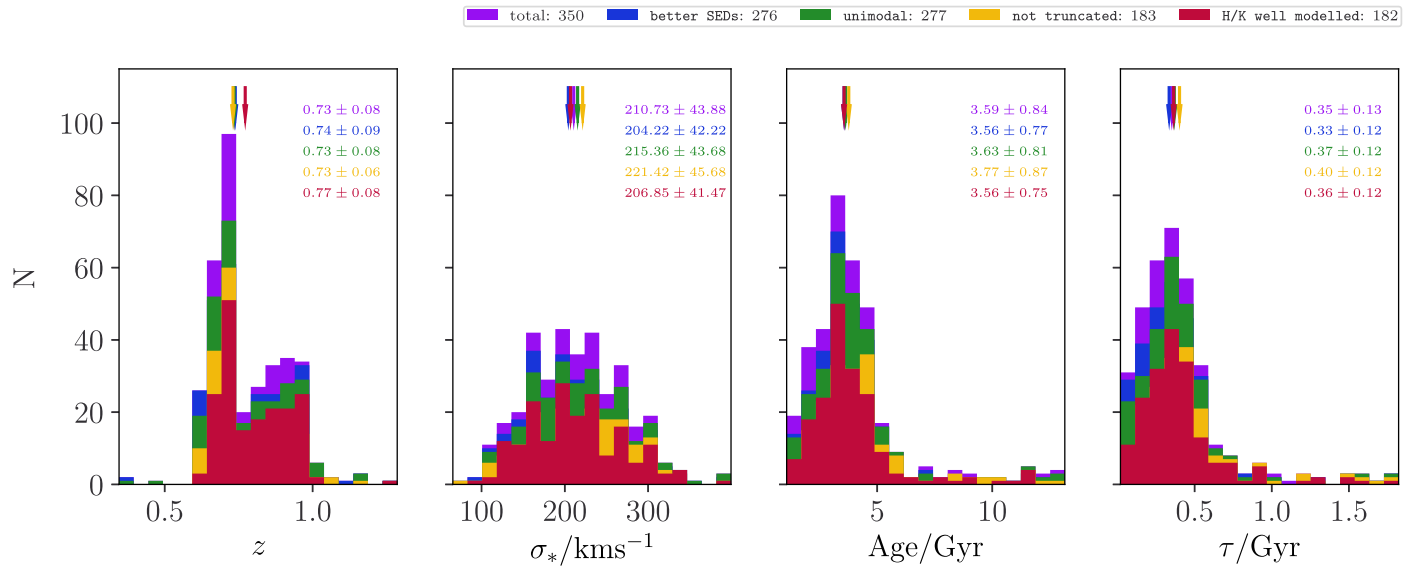
Figure 3. Distributions of redshift (z), stellar velocity dispersion ($\sigma_\star$), age, and formation timescale (τ) obtained from the fit of LEGA-C DR2 CCs with spectroscopic data alone (upper panels) and adding photometric data from Muzzin et al. (2013; lower panels). In each panel, we show the histograms of the full sample (purple) and those obtained when applying the quality flags described in Section 4.1, namely, `better SEDs` (blue), `unimodal` (green), `not truncated` (yellow), and `H/K well modeled` (red).

We find that the `not truncated` flag removes more galaxies in the lower age regime by increasing the median of the age from $\langle t \rangle = 4.1 \pm 1.5$ to 5.6 ± 2.4 Gyr and the value of τ from $\langle \tau \rangle = 0.5 \pm 0.3$ to 0.7 ± 0.3 Gyr, respectively, while the `unimodal` selection negligibly affects the shape of the posterior distribution of the derived parameters, as well as their median values. Though potentially improving its reliability, the `not truncated` and `unimodal` flags shrink the sample by approximately 20% and 50%–60%.

Poorly modeled Ca II H/K. The Ca II K and H lines, centered, respectively, at 3934 and 3969 Å rest frame (see Figure 4), are two prominent features in galaxy spectra. In galaxies dominated by an old stellar population, it is usually

found that the K line is deeper than the H line, this being opposite in the presence of young star-forming components (see Figure 5 in Moresco et al. 2018). In our analysis, we adopt the definition of H/K introduced by Fanfani (2019) that consists of measuring the ratio of two pseudo-Lick indices Ca II K and H, i.e., $H/K = I_H/I_K$. This technique is less sensitive to potential bias introduced by noise peaks in the spectrum with respect to using the H and K flux minima, i.e., $|H/K|_{min} = F_{min}(H)/F_{min}(K)$.

This diagnostic has been used to test the presence or absence of a contaminant population, therefore describing the purity of the selected sample (Moresco et al. 2018; Borghi et al. 2022a). In particular, Borghi et al. (2022a) found that $H/K < 1.2$ is
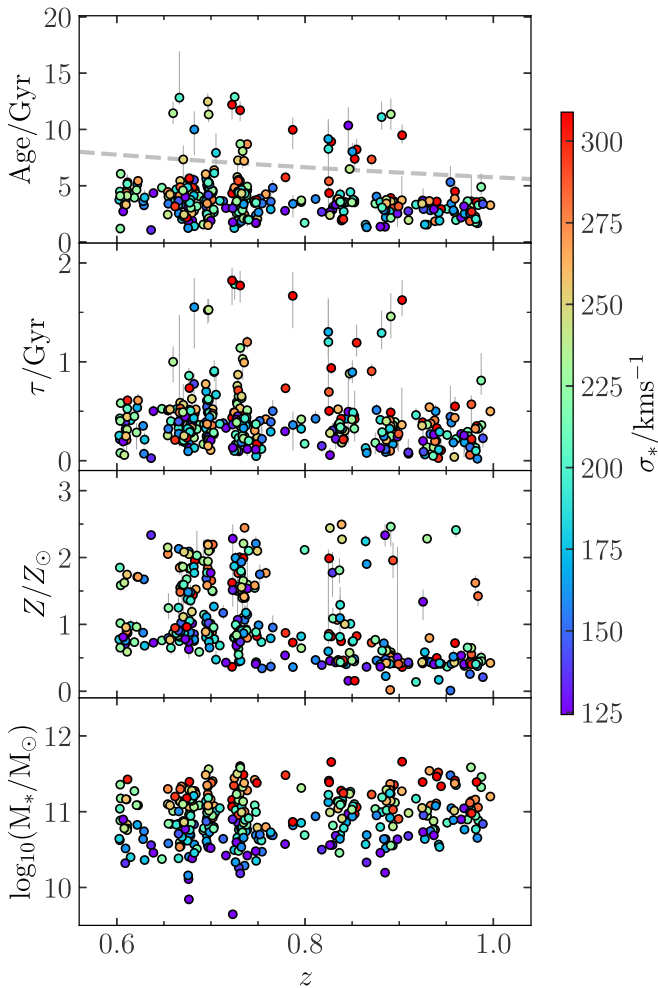
Figure 4. Distributions of stellar ages, star formation timescales (τ), metallicities (Z), and logarithmic stellar masses ($\log(M_\star/M_\odot)$) vs. z obtained from the full-spectrum fitting of 335 individual CCs in LEGA-C DR2. Each galaxy is color-coded by its stellar velocity dispersion ($\sigma_\star$). The first three panels span the entire parameter space explored; for a more detailed description, see Section 3.

safely equivalent to $|H/K|_{min} > 1$, and $H/K < 1.1$ well reproduces other selection criteria, including *NUVrJ* (Ilbert et al. 2013) and the $sSFR/yr < -11$ cut. They tested that the current sample of passive galaxies has a typical value of $H/K = 0.96 \pm 0.08$, validating the purity of the selection. We also do not observe any correlation between the galaxies' properties (especially age) and the H/K in both the observed and posterior spectra, indicating that no significant contribution from young stellar components is present in our passive galaxy sample. This also excludes the possible presence of galaxies that experienced recent rejuvenation events as found in Chauke et al. (2019).

It is, therefore, plausible to consider that the posterior spectra that do not adequately reproduce this feature are not completely appropriate fits and should be excluded. We calculate the H/K ratios in the observational LEGA-C DR2 spectra and our posterior spectra using PYLICK.[7] Then, we associate a flag with removing galaxies from the sample according to the following criterion: if the discrepancy between the observed and inferred

value is greater than 10%,

$$\frac{|H/K_{post} - H/K_{obs}|}{H/K_{obs}} > 10\%, \tag{8}$$

we consider that the feature has not been well reproduced, resulting in a potential deviation in the age estimation of the galaxy. We define the flag corresponding to this criterion as `H/K well modeled`. Applying this flag, we observe a considerable reduction in the long-tail shapes of the age and τ distributions in Figure 3, which clearly demonstrates the importance and validity of this criterion.

Inconsistency between photometric and spectroscopic data. The calibration of spectroscopic and photometric data is a complex process, and systematic differences between data obtained using different calibration pipelines are possible. To ensure a proper combination of the different sets of data, we must compare the photometric points (when available) in the wavelength region covered by the observed spectrum to the flux of the spectrum at the effective position of the corresponding photometric filters (see description in Section 2). If the difference between the two is significant, it means that there is an inconsistency between the photometric and spectroscopic points, and therefore these data cannot be fit jointly. We define the median absolute pull (MAP) between the photometric and spectral fluxes in the form of

$$MAP = Median\left(\frac{|f_{spec,i} - f_{phot,i}|}{\sqrt{\sigma^2_{f_{spec,i}} + \sigma^2_{f_{phot,i}}}}\right), \tag{9}$$

where the spectral fluxes are averaged over extremely narrow wavelength windows (10 pixels $\sim$6 Å) centered at the effective wavelength of the filters. We conservatively keep only the galaxies with an MAP $\leqslant$ 1. Such flagging is stringent enough to rule out most of the largest potential deviations. Throughout the paper, we refer to this specific flag as `better SEDs`. Applying this flag, we observe that the median of the age and $\sigma_\star$ are equivalent to the values when applying the `H/K well modeled` flag, even though the differences are not significant, still suggesting that the fluxes' inconsistency has a negative effect on simultaneously fitting spectroscopic and photometric data.

Inspecting Figure 3, we notice how in the case where only the spectrum is fitted, the various flags defined are crucial to significantly help reduce the tails of nonphysically large values of age (age > 7 Gyr) and τ (τ > 1 Gyr), which are severely affected by the age–τ degeneracy. This effect is especially evident by comparing the median values of each distribution as a function of the different flags applied, as also reported in the figure. At the same time, analyzing the distribution of the fit obtained from the joint analysis of the spectrum and photometry, we notice how the impact of the flagging is significantly smaller, and that the addition of the photometric bands per se helps in reducing the degeneracy between the parameters and obtaining well-converged fits with an extremely negligible fraction of points at high ages and τ. It also remains interesting to notice that despite wide and uninformative priors on age and τ, the derived best fits confirm the fact that these

---

[7] The code is available at https://gitlab.com/mmoresco/pylick/.

objects have been selected extremely accurately, and that they are old objects formed over relatively small timescales.

In conclusion, we decide to keep as our baseline for the analysis the fit that includes spectroscopic and photometric data without including any flagging, maximizing in this way both the accuracy of the results and the final statistics. In Section 5.2, we will discuss and quantify the impact of applying these flags on our cosmological result.

4.2. Galaxy Properties

Figure 4 presents the final constraints to the stellar population properties, namely, the best-fit stellar age, metallicity (Z), mass (M_*), and star formation timescale (τ), by assuming a DED SFH (see the last row of Table 1 for more details on the model ingredients and adopted priors). We use the light-weighted properties instead of the mass-weighted ones, considering that the latter are more sensitive to the choice of the SFH parameterization (Conroy 2013). Each galaxy is color-coded by its stellar velocity dispersion. Interestingly, even if do not bind the upper age value with a cosmological prior, we find that this population of galaxies qualitatively follows the descending trend predicted from the ΛCDM model assuming the Planck Collaboration et al. (2020) parameters, with less than 10% of galaxies higher than the reference ΛCDM boundary. The median age is $\langle t \rangle = 3.60 \pm 0.82$ Gyr . For comparison purposes only, when assuming a baseline ΛCDM model, this value corresponds to a typical formation time of ~ 3 Gyr after the Big Bang, or $z_f \sim 2.5$, in agreement with a wealth of literature data (e.g., Gallazzi et al. 2014; Belli et al. 2019; Carnall et al. 2019, 2022; Tacchella et al. 2022). In Section 5, we further study the age–(z) relation and its trends with $\sigma_\star$.

For the first time, we are able to quantitatively study the star formation timescale τ–redshift relation for this sample of CCs. Even if we adopt a wide uniform prior on $\tau \sim \mathcal{U}[0, 2]$ Gyr, we find a typical $\langle \tau \rangle = 0.36 \pm 0.13$ Gyr , with about 80% of the galaxies having $\tau < 0.5$ Gyr. Most importantly, from this analysis, we find no significant dependence on z. This is an additional confirmation that the current sample of passive galaxies is very homogeneous in its physical properties over different z. In addition, we do not find a statistically significant trend of τ with $\sigma_\star$. This is not in contradiction with the idea that more massive galaxies formed in shorter timescales (as expected from the downsizing scenario; Cowie et al. 1996). On the contrary, we are selecting the very massive and passive envelope of objects, so that we expect the shortest τ and no correlation with mass. This may also explain the reason why our SFHs are shorter than those derived by Chauke et al. (2018) on LEGA-C quiescent galaxies. But for a definitive answer, the impact of different SFH assumptions must be further assessed. Similar values of τ for quiescent galaxies at intermediate redshifts were also obtained by Pacifici et al. (2016), Carnall et al. (2019), and Tacchella et al. (2022).

We find stellar metallicities with slightly under solar values, $\langle Z/Z_\odot \rangle = 0.84 \pm 0.41$, in agreement with Borghi et al. (2022a), who found a typical $Z/Z_\odot \sim 1.1$ using Lick indices. This result further strengthens the idea that there exists a population of massive and passive galaxies that, at least up to $z \sim 0.8$, does not evolve significantly in its metal content and has values similar to those of its local counterparts (see also Thomas et al. 2011; Gallazzi et al. 2014; Onodera et al. 2015; Estrada-Carpenter et al. 2019). However, we observe an

evolution toward smaller Z with increasing redshift, as observed in Beverage et al. (2021) for 68 massive quiescent LEGA-C galaxies or Carnall et al. (2022) with VANDELS galaxies at $z \sim 1.2$. We traced that this effect is due to a degeneracy between metallicity and dust in the fit because it completely disappears when we remove that parameter from the fit. We also notice that, instead, the differential age measured is very stable, since the Hubble parameter derived in that configuration varies only by 1.1% with respect to our baseline, well below the currently estimated error. We discuss this point in the Appendix.

The stellar masses derived in the analysis correlate with the observed stellar velocity dispersion. This is a well-established result, usually interpreted with the idea that galaxies with a larger gravitational potential well are capable of retaining more gas and therefore forming more stars.

In conclusion, our sample of CCs shows ages and star formation timescales supporting the scenario that they must have formed at early epochs and with very short star formation events quickly exhausting their gas reservoirs and then evolved passively.

## 5. From Differential Ages to the Hubble Parameter

5.1. Binning Parameters

To apply the CC approach, we need to use the age–(z) relation obtained in our analysis to derive the differential age evolution Δt in a given redshift bin Δz. Since this measurement involves the estimation of a derivative, it is typically convenient, in the case of noisy data, to increase the S/N of the data by averaging different values, consequently having a more robust estimate of the differential age. This same approach has been adopted in most of the CC studies; see, e.g., Moresco et al. (2012), Moresco (2015), Moresco et al. (2016), and Borghi et al. (2022b).

Following the previous works by Moresco et al. (2016) and Borghi et al. (2022b), we decide to average our data not only as a function of redshift but also as a function of the velocity dispersion. This last step is particularly important on the one side, since it allows us to detect possible trends of the physical parameters as a function of $\sigma_\star$ (i.e., as a function of the stellar mass) but at the same time because, as highlighted by Thomas et al. (2011), stellar populations of different stellar masses correspond to populations formed at different times and over different timescales. Performing an analysis at an almost constant velocity dispersion (or stellar mass) ensures the homogeneity of the tracers compared and, as a consequence, a nonbiased determination of the Hubble parameter. For more details, see Moresco et al. (2022).

We note here that before binning and averaging our data, we further excluded 15 objects from our sample, since they had a redshift significantly different from the bulk of the population (see Figure 3); we therefore imposed a cut, $0.6 \leqslant z \leqslant 1.0$, ending up with 335 galaxies. From now on, all of the results will be referred to this sample.

Several different choices of binning can be adopted, including the type and number of bins, as well as the type of average statistics adopted. In particular, we can choose to divide the data into $N \times M$ bins of redshift and velocity dispersion, have bins of fixed widths or divided into equipopulated quantiles, and estimate within each bin the averaged quantities with different methods (mean, median,
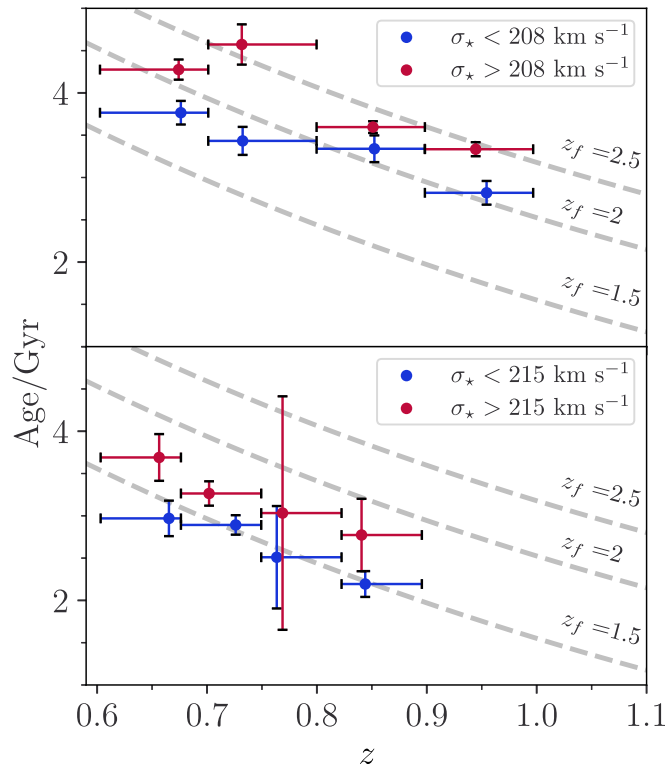
Figure 5. Median-binned age–redshift relations for our baseline results based on full-spectrum fitting (top) and for the Lick index analysis from Borghi et al. (2022b; bottom). The blue and red points represent the lower and higher $\sigma_\star$ bins, divided using the median value of each sample as the threshold. For each bin, the vertical error bars are the errors associated with the median ages, while horizontal bars denote the bin width. For illustrative purposes only, we include the redshift of formation (gray dashed lines) assuming a reference ΛCDM model from Planck Collaboration et al. (2020).

weighted mean). We must consider a trade-off between the benefit of avoiding uneven data distribution by using quantile bins and the benefit of improved population separation by using fixed bins. Additionally, we must use a sufficient number of bins to achieve both good statistics and an optimal sampling of the age–z trend. If the number is too large, the statistics of each bin deteriorate and create large oscillations; on the other hand, if the number is too small, the evolution trend is smoothed out.

We consider median statistics instead of an arithmetic (or weighted) average because it is less sensitive to outliers (including badly constrained galaxies; see Section 4.1). In particular, we decided to avoid the use of a weighted average because we observed a positive correlation between the estimated ages and their uncertainties, with younger galaxies having smaller uncertainties. Therefore, by using a weighted average, we would have biased our result toward smaller ages. We use the sampling error of the median in the form of $\sigma = \mathrm{MAD}/\sqrt{N}$, where MAD is the median absolute deviation, and N is the number of galaxies in that bin.

We test all of the possible choices for binning z and $\sigma_\star$, as well as the combinations of them, including setting the quantile or fixed binning type, taking reasonable values of binning size for $N_{z\mathrm{bin}}$ in $\{4, 2, 1\}$ and $N_{\sigma_\star\mathrm{bin}}$ in $\{2, 1\}$, as labeled in Figure 6. We do not use additional bins to ensure that each bin contains a sufficient number of galaxies. We have an average of approximately 40 galaxies per bin in the case of 4×2 bins that significantly decreases to 20 when the H/K selection is applied. After a careful comparison of the various options, we decide to consider as our baseline binning four fixed z bins combined with two quantile $\sigma_\star$ bins and median statistics, since it provides the best trade-off between a large enough redshift range probed, a separation in velocity dispersion allowing us to

study the mass effect, and the same number of bins to compare our results to Borghi et al. (2022b). We discuss the rationale of this choice in further detail, as well as quantify its impact on the results, in Section 5.2.

In Figure 5, we compare our baseline binned age(z) to the one obtained by Borghi et al. (2022b). As a first point, we observe an offset between the absolute ages estimated in the two methods of about 0.61 ± 0.05 Gyr. This difference can be explained and interpreted by taking into account the different SFHs adopted in the two analyses. In Borghi et al. (2022b), the theoretical models for the Lick indices were available only for SSP, while in this analysis, we assumed a more complex and realistic SFH, which is also one of the improvements of this analysis with respect to the previous one. The net effect is the bias in age observed.

It is, however, striking to observe the accuracy with which both derived ages evolve as a function of redshift. Qualitatively, they both follow extremely well the cosmological lines reported as a reference in the figure, demonstrating that despite the difference in the method, the difference in the assumed SFH, the slightly different threshold in $\sigma_\star$ adopted, and the different number of objects, the differential ages agree extremely well. This will be demonstrated quantitatively in the following section, but it is important to stress here that this is the first time that two different methods to derive differential ages on a common sample of pure massive and passive galaxies (CCs) have been performed. The agreement found between the trends of Δt is, therefore, an additional piece of evidence supporting the robustness of the CC method as a cosmological probe.

Additionally, we observe a distinct mass-downsizing pattern for which more massive galaxies ($\sigma_\star > 208 \, \mathrm{km \, s^{-1}}$) exhibit a
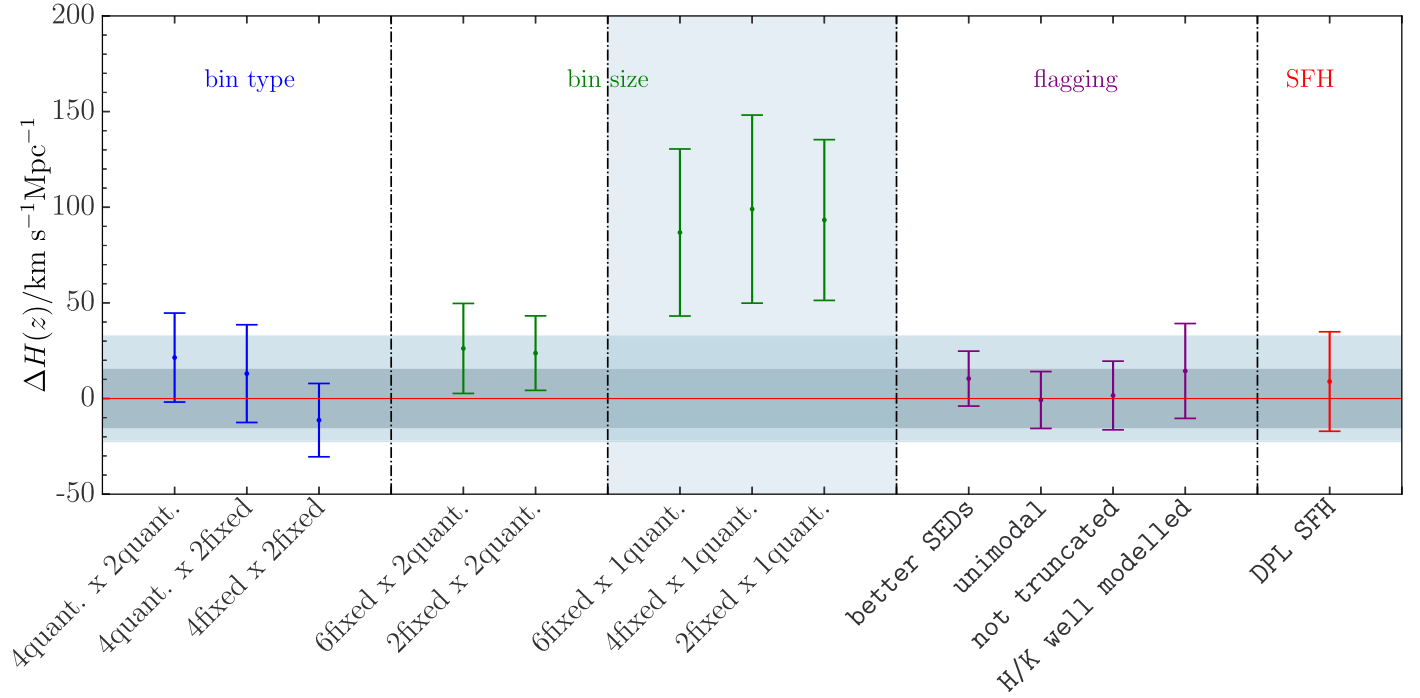
Figure 6. Difference between our final $H(z)$ measurement (obtained with four fixed z bins × two quantile $\sigma_\star$ bins) and the other values obtained by varying the bin settings, in particular the bin type (blue) and size (green), by applying different quality flags (violet) as described in Section 4.1 or fitting an alternative DPL SFH (red). The horizontal dark and light shaded regions represent the statistical and total uncertainty of the final $H(z)$, the latter defined as $\sqrt{\sigma_{\mathrm{stat.}}^2 + \sigma_{\mathrm{syst.}}^2}$. The values obtained without binning in $\sigma_\star$ (vertical shaded region) are the most significant contributors of the systematics error budget.

higher redshift of formation ($z_f \sim 2.5$) with respect to less massive ones ($z_f \sim 2$). Our z_f estimates are approximately 0.5 higher than those in Borghi et al. (2022b), still due to the use of a more extensive and realistic SFH (DED model) that allows the star formation to start earlier and persist over a longer period of time with respect to the SSP. Our results also achieve higher z and smaller errors of binned ages due to the use of a larger sample of galaxies (335) with respect to Borghi et al. (2022b; 140), which reduces statistical errors, particularly in the third z bin. With the same number of z bins, our result also gives a larger range of redshift, allowing us to probe the universe up to a slightly higher z.

5.2. Measuring H(z)

We compute $H(z)$ by using the binned ages and redshifts described in the previous section,

$$H(z) = -\frac{1}{(1+z)}\frac{\Delta z}{\Delta t}. \qquad (10)$$

To minimize the impact of fluctuations in the data, we do not use consecutive bins to calculate Δz and Δt but rather a difference approach based on nonadjacent bins, estimating the difference, in a given $\sigma_\star$ bin, between the ith and the $(i + N/2)$th point, where N is the number of redshift bins defined. As presented in Section 5.1, we use two types of bin: fixed and quantile (i.e., flexible to ensure an equal number of objects in each bin). This strategy requires making an even number of redshift bins to avoid covariance between results caused by multiple uses of the same data point. This approach also allows us to estimate the difference between points where the expected age evolution is larger than the associated error, making the

estimate of Δt less noisy and more robust. This differential approach of the CC method plays a crucial role in minimizing the rejuvenation in the SFH (Moresco et al. 2022).

We perform this evaluation in each $\sigma_\star$ regime, obtaining $(N_{\mathrm{bin},\sigma_\star} \times N_{\mathrm{bin},z})/2$ Hubble parameter measurements. Finally, these values are combined to get a single and more accurate estimate of $H(z)$ with an inverse variance–weighted average (as also done in, e.g., Moresco et al. 2016; Borghi et al. 2022b).

The different choices of how to bin and select our data, as well as the assumed SFH, are potential sources of systematic uncertainties for the final $H(z)$. In our analysis, we do not account for other systematics introduced by other assumptions of the stellar population synthesis (SPS) model, as we discuss in Section 6 (for a detailed treatment, see Moresco et al. 2020, 2022). In summary, starting from our baseline result, we estimate the impact on the cosmological results by adopting different choices of binning (Section 5.1), different flagging methods (Section 4.1), or a different SFH assumption that decouples the rising and declining slopes of the SFH (i.e., DPL; see Section 3). This will allow us to estimate the systematic errors due to these effects to be associated with our measurement. The results are shown in Figure 6.

First of all, we observe that the configurations contributing the most to a systematic difference in $H(z)$ are those in which all galaxies are averaged together in a redshift bin independently of their $\sigma_\star$. The larger shift underlines even more the need to perform the analysis of CC by carefully selecting the sample in bins of velocity dispersion (or stellar mass); otherwise, the assumption of having a homogeneous sample of chronometers is dropped, and mixing different galaxy populations will exacerbate the progenitor bias (van Dokkum et al. 2000). As shown in Figure 6, we end up smoothing the evolutionary trend, obtaining a higher $H(z)$ and a larger scatter,
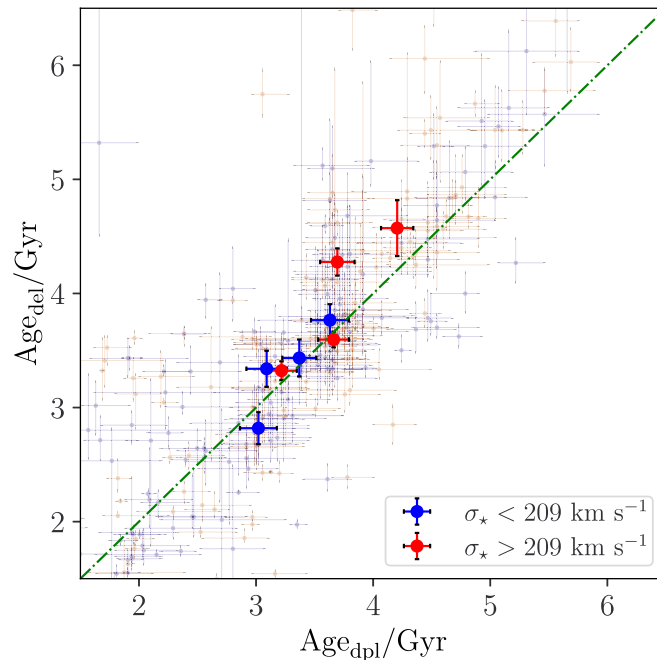
Figure 7. Galaxy ages fitted by a full spectroscopic and photometric fitting based on the DED model vs. those fitted under the same fitting configurations but based on the DPL model. The thin error bars represent measurements of individual massive and passive galaxies selected in LEGA-C DR2, while the thick error bars are the binned results (obtained with the four fixed z bins × two quantile $\sigma_\star$ bins), which are both colored by their $\sigma_\star$, with the lower bins in blue and higher bins in red. The green dashed–dotted line marks the diagonal direction.

resulting in larger statistical uncertainties. We also note that by using (equipopulated) quantile bins in z, we obtain higher $H(z)$ values with respect to fixed bins. This behavior may be explained by the uneven redshift distribution of our galaxies (see Figure 1). In particular, because there are fewer high-redshift galaxies, the high-redshift quantile bins span a much wider interval, thus flattening the age–(z) relation and, ultimately, increasing $H(z)$ and its associated uncertainty. On the contrary, the $\sigma_\star$ distribution is approximately Gaussian, which makes the result of quantile and fixed $\sigma_\star$ bins not significantly different.

As for the number of z bins, the results show that a smaller or larger number of bins produce a higher $H(z)$, which is reasonable because, due to the redshift distribution, a smaller number of bins does not allow one to correctly map the slope of the age–redshift relation, since the larger dz and lower statistics at high z would artificially flatten the median age(z). Besides, by taking more bins, the data will be noise-dominated.

Even though flagging posteriors slightly changes the value of $H(z)$, all of the related results are compatible with our baseline result as shown in Figure 6.

The various choices of the SFH could further contribute to systematic uncertainties in the measurement of $H(z)$. To address this point, we fit our sample with a different, more flexible SFH model, DPL (see Section 3), commonly used in other BAGPIPES analyses (Carnall et al. 2018). To evaluate the difference brought on by a change in the SFH, we solely alter the SFH assumed and keep the other fitting configuration unchanged. In Figure 7, we make a direct comparison between the ages obtained using the two models, showing that the ages estimated with the two models are compatible. To quantitatively assess the impact of choosing a different SFH on our result, we estimate the Hubble parameter with the DPL SFH. With all other configurations of analyses unchanged, we obtain $H(z = 0.80) = 122.0 \pm 21.1$ km s^{-1} Mpc^{-1} using the results by

fitting the DPL model, showing a 7.9% difference compared to our baseline $H(z)$. We take this as an estimation of the systematic uncertainty caused by the choice of the SFH model.

To assess the systematic error, we therefore consider our baseline result and quantify how much the results are perturbed by three sources of systematics, namely, varying the binning scheme and applied quality flags and assuming a different DPL SFH. We estimate the median difference between our baseline $H(z)$ and the measurements obtained from each source, taking

$$\sigma_{\mathrm{syst},j} = \mathrm{median}(H(z)_j - H(z)_{\mathrm{base}} - \Delta H_{\mathrm{model}}). \quad (11)$$

In this equation, we need to account for the difference caused by redshift evolution, $\Delta H_{\mathrm{model}} = H_{\mathrm{model}}(z_{\mathrm{base}}) - H_{\mathrm{model}}(z_j)$, where the choice of the assumed cosmological model negligibly affects the case of minuscule redshift difference. We compute the total systematic uncertainty by summing each contribution in quadrature and calculating the upper and lower $\sigma_{\mathrm{syst.\,tot.}}$ separately.

In summary, we obtain a new cosmology-independent measurement of $H(z) = 113.1 \pm 15.1(\mathrm{stat.})^{+29.1}_{-11.3}(\mathrm{syst.})$ km s^{-1} Mpc^{-1} at $z = 0.80$. Our measurement is consistent with the $H(z = 0.75) = 98.8 \pm 33.6$ km s^{-1} Mpc^{-1} that Borghi et al. (2022b) obtained. We notice that the statistical error decreases from 24.8 to 15.1 km s^{-1} Mpc^{-1}, i.e., by a factor of approximately 0.6, equivalent to the inverse of $\sqrt{335/140}$ due to the increasing number of CCs used for our $H(z)$ measurement. The biggest contribution to this uncertainty is given by the binning scheme, in particular when $H(z)$ is computed without separating the galaxies into two $\sigma_\star$ subsamples. By excluding this contribution, the upper systematical error decreases to 26.1 km s^{-1} Mpc^{-1}. In Figure 8, we compare our final result with all of the currently available $H(z)$, finding a noticeable consistency.
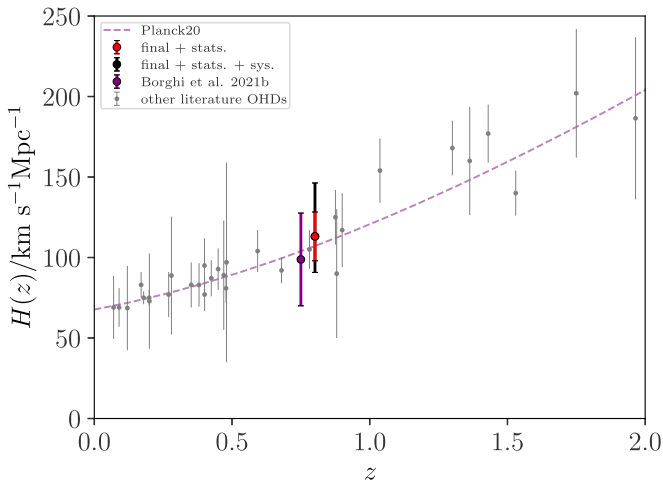
Figure 8. Final $H(z)$ value obtained from full spectral fitting of 335 CCs in LEGA-C DR2 with statistical (red) and total (black) uncertainty. The violet point is the value obtained by Borghi et al. (2022b) via Lick index analysis of 140 galaxies of this data set. The gray points are all of the other OHD available from the literature (Jimenez et al. 2003; Simon et al. 2005; Stern et al. 2010; Moresco et al. 2012; Zhang et al. 2014; Moresco 2015; Moresco et al. 2016; Ratsimbazafy et al. 2017). For illustrative purposes only, we include the $H(z)$ prediction assuming a ΛCDM model with Planck Collaboration et al. (2020) parameters.

6. Conclusions

In this paper, we analyze a sample of 350 massive and passive galaxies mostly (95%) at $0.6 \lesssim z \lesssim 1.0$ extracted from LEGA-C DR2 in Borghi et al. (2022a), deriving their physical properties from a full spectral fitting analysis. Given that the ultimate goal of this work is apply the CC method with this data set, it was optimized and thoroughly tested to minimize the possible contamination of the sample by young star-forming objects. The derived age–(z) relation is then used to constrain the differential ages dt and provide a new estimate of the Hubble parameter $H(z)$. Our analysis will also allow us to compare, for the first time on the same data set, the differential ages dt derived with two different and independent methods, namely, Lick indices and full spectral fitting, and to investigate and validate the capability of the CC approach to robustly derive $H(z)$.

Here we utilize the public code BAGPIPES (Carnall et al. 2018) to derive stellar ages, metallicities, and SFH fitting for both the spectroscopic data alone and the spectroscopic and photometric data jointly for all of the individual galaxies in our sample. Our main results are summarized as follows.

1. We first extend BAGPIPES by removing the cosmological prior on the derived ages to avoid possible biases on our cosmological results due to the assumption of a fiducial cosmology. We also adopt flat uninformative priors on all of the derived quantities, namely, the stellar age, metallicity, and SFH. We then explore the dependence of our results on the SFH assumed, parameters included in the fit, and priors considered. We opt to use a DED SFH, improving with respect to the analysis of Borghi et al. (2022a) where SSP is assumed, but minimizing the number of free parameters for the functional form of the SFH, since we verified that the gain in the quality of the fit was marginal with other choices.

2. We find the results obtained from the fit to the spectroscopy alone to be less accurate and more scattered than the results obtained by fitting the combination of spectroscopy and photometry, in particular with larger tails toward higher ages and τ. We define a set of indicators of the quality of the fit and convergence criteria based on the inspection of the posterior distribution and the accuracy with which the best fit was reproducing specific observational features in the spectrum, namely, the Ca II H/K known to be correlated with potential episodes of recent star formation. We demonstrate that the nonphysical scatter in the derived parameter obtained using only spectroscopic data can be lifted by applying masks defined by these indicators.

3. We observe that the inclusion of photometric data (21 bands in this analysis) allows the fit to converge correctly even without applying the convergence criteria previously discussed, reducing the degeneracy between parameters. As a consequence, in this framework, we are able to maximize the final number of objects with a correct fit, and we decide to consider this as the baseline of our analysis.

4. We find that the measured age–(z) relation is well compatible with cosmological aging as a function of redshift, even with assumed a flat prior on age $\in \mathcal{U}(0, 20)$ Gyr. Our results also present a clear downsizing trend when divided into two bins of velocity dispersion, with galaxies with $\sigma_\star > 108$ km s^{-1} having a formation redshift $z_f \sim 2.5$ and the ones with $\sigma_\star < 108$ km s^{-1} having a formation redshift $z_f \sim 2$. Even though we consider a significantly wider prior in our analysis, these galaxies show very short star formation timescales with a median value of $\langle \tau \rangle = 0.36 \pm 0.13$.

5. The average measured stellar metallicity is $\langle Z/Z_\odot \rangle = 0.84 \pm 0.41$, with a small hint of evolution as a function of redshift. We prove that this tension or fitted evolution is due to the degeneracy between the metallicity and dust in the fit and demonstrate that it has an almost negligible effect on the differential age.

6. We compare for the first time the stellar ages derived from two very different and independent methods applied to the same sample, the full-spectrum fitting and the Lick index analysis. We find that the absolute ages derived present an offset of 0.61 ± 0.05 Gyr, which can be understood by recalling that the Lick index models assume an idealized SSP SFH that slightly biases the absolute values toward younger ages. The agreement, however, between the differential ages is striking, and it is important to underline here that the CC approach is based on the measurement of dz/dt, which perfectly agrees within the errors in the two measurements. This result is particularly important because it demonstrates the robustness of the method and the stability of the dt measurement, confirming that it can be derived with significantly less bias than absolute ages.

7. From the analysis of the binned age–(z) relation, we derive a new $H(z)$ measurement, $H(z = 0.80) = 113.1 \pm 15.1$(stat.). We verify that our result is fully compatible with the one by Borghi et al. (2022b), even if at a slightly larger redshift and with a slightly smaller statistical error due to the different number of objects in the final sample used by the two methods (in Borghi et al.

13

2022b, to ensure homogeneity in the analysis, we decided to consider in the final sample only the spectra for which the same number of spectral features were observable). We also test that our result is consistent with other literature OHD, as well as with the prediction of a ΛCDM model assuming the Planck Collaboration et al. (2020) cosmological parameters.

8. We assess the systematics involved in the results by varying the methods with which the binned age–(z) relations are derived, changing the number of bins, the method to estimate the average value, and the assumed SFH model in the fit and testing the application of the masks described above. We estimate a systematic error of $+29.1 - 11.3$(syst.) km s^{-1} Mpc^{-1}, mainly dominated by the large variation in the results obtained when the sample is not divided into two $\sigma_\star$ (or stellar mass) bins, suggesting that an analysis in specific ranges of masses is fundamental to ensure homogeneity in the formation of the CCs considered.

9. In the end, we obtain a measurement of the Hubble parameter $H(z) = 113.1 \pm 15.1$(stat.)$^{+29.1}_{-11.3}$(syst.) at $z = 0.80$.

We underline that, since the samples used in this analysis and the one of Borghi et al. (2022b) are drawn from the same parent sample, using them in combination should be avoided, since the measurements will be highly covariant. We also underline that in the current analysis, we decided not to explore the further dependence of our result on other assumptions of the SPS models. Regarding the dependence on different SFHs, we verified that within BAGPIPES, the SFH choice is somehow limited (we could have chosen among SSP, DED, and DPL, but the SSP yields a discrete pattern on galaxy ages, weakening the reliability of the differential ages obtained, which, however, can be improved by a rerun of the SPS on more refined grids); therefore, it would not have allowed a full estimate of this effect. Moreover, the fit obtained with the DPL SFH provided similar results to the ones obtained here but with a higher number of free parameters, not justifying the choice of that SFH in our case. In the end, we chose the DED model as our baseline and the DPL for evaluating the systematic uncertainty caused by the SFH choice.

Further investigation is crucial to go beyond analytic forms of SFHs. We notice that nonparametric SFHs (e.g., Leja et al. 2019) could be more flexible options than these analytic approximations in describing the full diversity of SFH shapes, and they are becoming popular alternatives to parametric ones. Therefore, we acknowledge that to assess systematic effects, they could be interesting alternatives to exploit. We explored this possibility using the latest update of BAGPIPES, which includes the possibility of using a nonparametric SFH proposed by Leja et al. (2019), considering a model with a continuity prior on $\Delta \log(\mathrm{SFR})$ between adjacent time bins (seven bins in total). The results we obtained are extremely encouraging and point toward the fact that the SFH uncertainty is currently not dominant in our analysis. We found that the Hubble parameter estimated considering a nonparametric SFH is compatible within 0.27σ with respect to the one we derive in our analysis. A larger statistical uncertainty is also expected in this case, since a more flexible SFH with a larger number of free parameters is considered. However, further checks and verifications that go beyond the scope of this paper are needed before including this result as a further systematic uncertainty in our analysis, and we defer it to a later paper.

Dry mergers of less massive galaxies hosting younger stellar populations may bias the light-weighted age estimation toward younger ages. However, this effect is expected to be subdominant, since this analysis is based on differential ages and spans a limited redshift interval (Moresco et al. 2012). While the sample selection criteria in Section 2 are aimed at minimizing contamination of the young component, a residual, even if minor, evolution could bias our measurement. In Moresco et al. (2018), a recipe was provided to include an error contribution due to this effect in the covariance matrix of the $H(z)$ measurement, which we quantify to be negligible in this sample.

The rejuvenation in the SFH could introduce bias in the measurement of the differential ages. This was addressed in detail in Moresco et al. (2012, 2018), where it quantified the impact of these effects on the Hubble parameter (see, in particular, Appendix A.1 of Moresco et al. 2012, and Sections 5 and 6 of Moresco et al. 2018). The main point to stress here is that the selection process in Section 2 and the differential approach of the CC method in Section 5 play a crucial role in minimizing this effect. Moreover, the systematic uncertainty originating from the binning method takes into account the potential progenitor bias, as we explain in Section 5.2.

To include in the current measurement a proper full systematic covariance matrix, we therefore suggest that the reader follow the procedure described in detail in Moresco et al. (2022, 2020), including the missing statistical effects not already included in this analysis.

In conclusion, this work provides a further important piece of evidence supporting the robustness of the CC method as a cosmological probe, showing the potential of the full spectral fitting approach as another different method to derive the relative ages of massive and passive galaxies. It is interesting to notice here that our sample is almost a factor of 2 larger than the final sample used by Borghi et al. (2022b), and the statistical error between the two measurement scales as expected as $\sqrt{N}$. This is very promising in the view of several current (SDSS BOSS Data Release 16; Ahumada et al. 2020) and incoming (such as Euclid; Laureijs et al. 2011; Wang et al. 2019) spectroscopic surveys that will significantly improve the census of massive and passive galaxies, especially at $z > 1$.

Appendix
The Dust–Metallicity Degeneracy

In the derived properties of the passive sample that is analyzed with the baseline configuration described in Section 3, we observe a slight evolution of metallicity as a function of redshift (as shown in the bottom panel of Figure 9), which appears to contradict the pure passive selection assumption of our sample. However, the assumption is supported by the results of Borghi et al. (2022a) that no evident evolution in metallicity and stellar mass is found on the same sample. Besides, we notice here that we also observe no evolution in the stellar mass in this case.

We find that such evolution is due to a degeneracy between metallicity and dust in the fit, since, as shown in the top panel of Figure 9, the evolution completely disappears when we remove that parameter from the fit. We find stellar metallicities with slightly supersolar values, $\langle Z/Z_\odot \rangle = 1.44 \pm 0.56$, in agreement with Borghi et al. (2022a), who found typical $Z/Z_\odot \sim 1.1$ using Lick indices. The metallicities show a clear downsizing pattern that, at each cosmic epoch, the stellar populations hosted in galaxies with higher mass are more metal-rich. In this configuration, we obtain $H(z=0.80) = 111.8 \pm 14.2$ km s^{-1} Mpc^{-1}, supporting the differential age measured is very stable since the estimated Hubble parameter varies only by 1.1% comparing to our baseline measurement, well below the currently estimated error. Since the main results are not affected, we decide to keep the current analysis as our baseline, as it allows for a wider exploration of the parameter space.
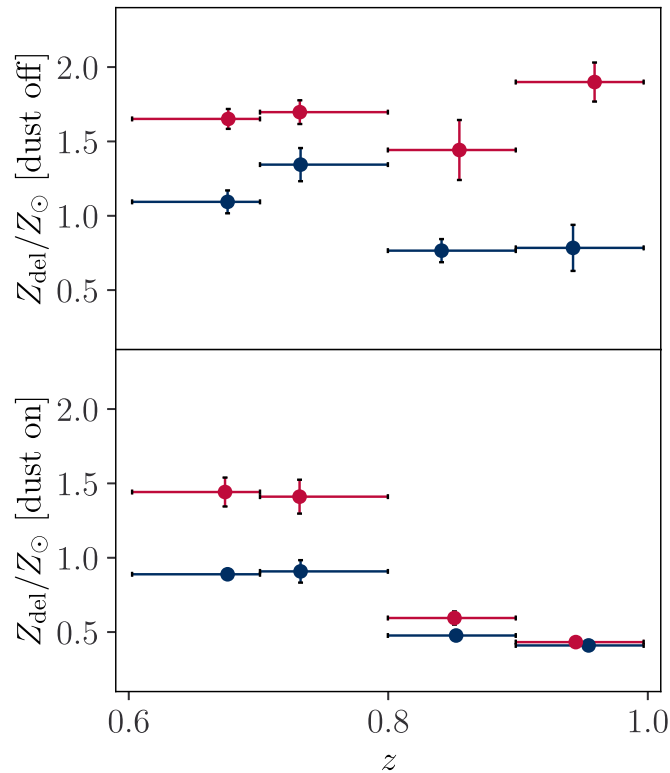
Figure 9. Median-binned metallicity–redshift relations for our baseline results based on a full-spectrum fitting that contains a dust model (bottom; Carnall et al. 2018) and for the fitting under the same configuration but with the dust model switched off (top). The blue and red points represent the lower and higher $\sigma_\star$ bins, divided using the median value of each sample as the threshold. For each bin, the vertical error bars are the errors associated with the median ages, while the horizontal bars denote the bin width.

ORCID iDs

Kang Jiao ⦿ https://orcid.org/0000-0003-0167-9345
Nicola Borghi ⦿ https://orcid.org/0000-0002-2889-8997
Michele Moresco ⦿ https://orcid.org/0000-0002-7616-7136
Tong-Jie Zhang ⦿ https://orcid.org/0000-0002-3363-9965

References

Abbott, B. P., Abbott, R., Abbott, T. D., et al. 2017, Natur, 551, 85
Abdalla, E., Abellán, G. F., Aboubrahim, A., et al. 2022, JHEAp, 34, 49
Ahumada, R., Prieto, C. A., Almeida, A., et al. 2020, ApJS, 249, 3
Allen, S. W., Evrard, A. E., & Mantz, A. B. 2011, ARA&A, 49, 409
Astropy Collaboration, Price-Whelan, A. M., Sipőcz, B. M., et al. 2018, AJ, 156, 123
Bartelmann, M., & Schneider, P. 2001, PhR, 340, 291
Belli, S., Newman, A. B., & Ellis, R. S. 2019, ApJ, 874, 17
Benitez, N., Gaztanaga, E., Miquel, R., et al. 2009, ApJ, 691, 241
Bennett, C. L., Halpern, M., Hinshaw, G., et al. 2003, ApJS, 148, 1
Betoule, M., Kessler, R., Guy, J., et al. 2014, A&A, 568, A22
Beverage, A. G., Kriek, M., Conroy, C., et al. 2021, ApJL, 917, L1
Borghi, N., Moresco, M., Cimatti, A., et al. 2022a, ApJ, 927, 164
Borghi, N., Moresco, M., & Cimatti, A. 2022b, ApJL, 928, L4
Bruzual, G., & Charlot, S. 2003, MNRAS, 344, 1000
Buchner, J., Georgakakis, A., Nandra, K., et al. 2014, A&A, 564, A125
Calzetti, D., Armus, L., Bohlin, R. C., et al. 2000, ApJ, 533, 682
Carlstrom, J. E., Ade, P. A. R., Aird, K. A., et al. 2011, PASP, 123, 568
Carnall, A. C., McLure, R. J., Dunlop, J. S., et al. 2019, MNRAS, 490, 417
Carnall, A. C., McLure, R. J., Dunlop, J. S., et al. 2022, ApJ, 929, 131
Carnall, A. C., McLure, R. J., Dunlop, J. S., & Dave, R. 2018, MNRAS, 480, 4379
Charlot, S., & Fall, S. M. 2000, ApJ, 539, 718
Chauke, P., van der Wel, A., Pacifici, C., et al. 2019, ApJ, 877, 48
Chauke, P., Wel, A. v. d., Pacifici, C., et al. 2018, ApJ, 861, 13
Cole, S., Percival, W. J., Peacock, J. A., et al. 2005, MNRAS, 362, 505
Conroy, C. 2013, ARA&A, 51, 393
Cowie, L. L., Songaila, A., Hu, E. M., & Cohen, J. G. 1996, AJ, 112, 839
Davis, T. 2019, Sci, 365, 1076
Di Valentino, E., Mena, O., Pan, S., et al. 2021, CQGra, 38, 153001
Eisenstein, D. J., Zehavi, I., Hogg, D. W., et al. 2005, ApJ, 633, 560
Estrada-Carpenter, V., Papovich, C., Momcheva, I., et al. 2019, ApJ, 870, 133
Fanfani, V. 2019, PhD thesis, Univ. Bologna
Farr, W. M., Fishbach, M., Ye, J., & Holz, D. E. 2019, ApJL, 883, L42
Ferland, G. J., Chatzikos, M., Guzmán, F., et al. 2017, RMxAA, 53, 385
Freedman, W. L., & Madore, B. F. 2010, ARA&A, 48, 673
Gallazzi, A., Bell, E. F., Zibetti, S., Brinchmann, J., & Kelson, D. D. 2014, ApJ, 788, 72
Harris, C. R., Millman, K. J., van der Walt, S. J., et al. 2020, Natur, 585, 357
Holz, D. E., & Hughes, S. A. 2005, ApJ, 629, 15
Hubble, E. 1936, The Realm of the Nebulae (New Haven, CT: Yale Univ. Press)
Hunter, J. D. 2007, CSE, 9, 90
Ilbert, O., McCracken, H. J., Le Fèvre, O., et al. 2013, A&A , 556, A55
Jimenez, R., & Loeb, A. 2002, ApJ, 573, 37
Jimenez, R., Verde, L., Treu, T., & Stern, D. 2003, ApJ, 593, 622
Laigle, C., McCracken, H. J., Ilbert, O., et al. 2016, ApJS, 224, 24
Laureijs, R., Amiaux, J., Arduini, S., et al. 2011, arXiv:1110.3193
Le Fèvre, O., Saisse, M., Mancini, D., et al. 2003, Proc. SPIE, 4841, 1670
Leja, J., Carnall, A. C., Johnson, B. D., Conroy, C., & Speagle, J. S. 2019, ApJ, 876, 3
Ma, C., & Zhang, T.-J. 2011, ApJ, 730, 74
Moresco, M. 2011, PhD thesis, Univ. Bologna, http://amsdottorato.unibo.it/3725/
Moresco, M. 2015, MNRAS, 450, L16
Moresco, M., Amati, L., Amendola, L., et al. 2022, LRR, 25, 1
Moresco, M., Cimatti, A., Jimenez, R., et al. 2012, JCAP, 2012, 006
Moresco, M., Jimenez, R., Cimatti, A., & Pozzetti, L. 2011, JCAP, 2011, 045
Moresco, M., Jimenez, R., Verde, L., et al. 2018, ApJ, 868, 84
Moresco, M., Jimenez, R., Verde, L., Cimatti, A., & Pozzetti, L. 2020, ApJ, 898, 82
Moresco, M., Pozzetti, L., Cimatti, A., et al. 2013, A&A, 558, A61
Moresco, M., Pozzetti, L., Cimatti, A., et al. 2016, JCAP, 2016, 014
Moresco, M., Verde, L., Pozzetti, L., Jimenez, R., & Cimatti, A. 2012, JCAP, 2012, 053

15

Muzzin, A., Marchesini, D., Stefanon, M., et al. 2013, ApJS, 206, 8
Onodera, M., Carollo, C. M., Renzini, A., et al. 2015, ApJ, 808, 161
Pacifici, C., Kassin, S. A., Weiner, B. J., et al. 2016, ApJ, 832, 79
Peng, Y.-j., Lilly, S. J., Kovac, K., et al. 2010, ApJ, 721, 193
Percival, W. J., Baugh, C. M., Bland-Hawthorn, J., et al. 2001, MNRAS, 327, 1297
Perlmutter, S., Aldering, G., Goldhaber, G., et al. 1999, ApJ, 517, 565
Pozzetti, L., Bolzonella, M., Zucca, E., et al. 2010, A&A, 523, A13
Planck Collaboration, Ade, P. A. R., Aghanim, N., et al. 2014, A&A, 571, A16
Planck Collaboration, Aghanim, N., Akrami, Y., et al. 2020, A&A, 641, A6
Ratsimbazafy, A. L., Loubser, S. I., Crawford, S. M., et al. 2017, MNRAS, 467, 3239
Riess, A. G. 2020, NatRP, 2, 10
Riess, A. G., Filippenko, A. V., Challis, P., et al. 1998, AJ, 116, 1009
Schutz, B. F. 1986, Natur, 323, 310
Scolnic, D. M., Jones, D. O., Rest, A., et al. 2018, ApJ, 859, 101
Simon, J., Verde, L., & Jimenez, R. 2005, PhRvD, 71, 123001
Smoot, G. F., Bennett, C. L., Kogut, A., et al. 1992, ApJL, 396, L1
Stern, D., Jimenez, R., Verde, L., Kamionkowski, M., & Stanford, S. A. 2010, JCAP, 2010, 008
Straatman, C. M. S., Wel, A. v. d., Bezanson, R., et al. 2018, ApJS, 239, 27
Sullivan, M., Guy, J., Conley, A., et al. 2011, ApJ, 737, 102
Suzuki, N., Rubin, D., Lidman, C., et al. 2012, ApJ, 746, 85
Swetz, D. S., Ade, P. A. R., Amiri, M., et al. 2011, ApJS, 194, 41
Tacchella, S., Conroy, C., Faber, S. M., et al. 2022, ApJ, 926, 134
Thomas, D., Maraston, C., & Johansson, J. 2011, MNRAS, 412, 2183
van Dokkum, P. G., Franx, M., Fabricant, D., Illingworth, G. D., & Kelson, D. D. 2000, ApJ, 541, 95
Verde, L., Treu, T., & Riess, A. G. 2019, NatAs, 3, 891
Virtanen, P., Gommers, R., Oliphant, T. E., et al. 2020, NatMe, 17, 261
Wang, Y., Dickinson, M., Hillenbrand, L., et al. 2019, arXiv:1909.00070
Weaver, J. R., Kauffmann, O. B., Ilbert, O., et al. 2022, ApJS, 258, 11
Williams, R. J., Quadri, R. F., Franx, M., van Dokkum, P., & Labbe, I. 2009, ApJ, 691, 1879
Wu, Q., Yu, H., & Wang, F. Y. 2020, ApJ, 895, 33
Zhang, C., Zhang, H., Yuan, S., et al. 2014, RAA, 14, 1221
Zhang, T.-J., Ma, C., & Lan, T. 2010, AdAst, 2010, 184284